Edinburgh Research Explorer

Water vapor uptake into hygroscopic lithium bromide desiccant droplets: Mechanisms of droplet growth and spreading

1 **Water vapor uptake into hygroscopic lithium bromide desiccant droplets:**

2 **Mechanisms of droplet growth and spreading**

3 Zhenying Wang[ab], Daniel Orejon[†ab], Khellil Sefiane[c], Yasuyuki Takata[‡ab]

4 a International Institute for Carbon-Neutral Energy Research (WPI-I²CNER), Kyushu University, Fukuoka 819-0395, Japan

5 b Department of Mechanical Engineering, Thermofluid Physics Laboratory, Kyushu University, Fukuoka 819-0395, Japan

6 c School of Engineering, Institute for Multiscale Thermofluids, University of Edinburgh, King's Buildings, Mayfield Road, Edinburgh

7 EH9 3JL, United Kingdom

8 Corresponding author: † orejon.daniel@heat.mech.kyushu-u.ac.jp; ‡ takata@mech.kyushu-u.ac.jp.

9 **ABSTRACT**

10 The study of vapor absorption into liquid desiccant droplets is of general relevance to a better

11 understanding and description of vapor absorption phenomena occurring at the macroscale as well as

12 for practical optimization of dehumidification and refrigeration processes. Hence, in the present work,

13 we provide the first systematic experimental study on the fundamentals of vapor absorption into

14 liquid desiccant at the droplet scale, which initiates a novel avenue for the research of hygroscopic

15 droplet growth. More specifically we address the behavior of lithium bromide-water droplets on

16 hydrophobic PTFE and hydrophilic glass substrates under controlled ambient conditions. Driven by

17 the vapor pressure difference between the ambient air and the droplet interface, desiccant droplets

18 absorb water vapor and increase in volume. To provide further insights on the vapor absorption

19 process, the evolution of the droplet profile is recorded using optical imaging and relevant profile

20 characteristics are extracted. Results show that, even though the final expansion ratio of droplet

21 volume is only function of relative humidity, the dynamics of contact line and the absorption rate are

22 found to differ greatly when comparing data with varying substrate wettability. Droplets on

23 hydrophilic substrates show higher absorption kinetics and reach equilibrium with the ambient much

24 faster than those on hydrophobic substrates. This is attributed to the absorption process being

25 controlled by solute diffusion on the droplet side and to the shorter characteristic length for the solute

26 diffusion on hydrophilic substrates. Moreover, the apparent droplet spreading process on hydrophilic

27 substrates when compared to hydrophobic ones is explained based on a force balance analysis near

28 the triple contact line, by the change of liquid-vapor surface tension due to the increase in water

29 concentration, and assuming a development of a precursor film.

30 **Keywords**: liquid desiccant, spreading, surface wettability, droplet dynamics, vapor absorption

1. INTRODUCTION

Droplet evaporation is a widely observed phenomenon in nature, and has been applied in several industrial and biological fields from ink-jet printing [1] and thin film coating [2,3], to DNA stretching and disease diagnosis [4]. In recent years, an increasing number of investigations have been carried out on the effect of ambient pressure [5,6], ambient temperature and humidity [7,8], as well as, substrate wettability [9,10], thermal conductivity and temperature [11,12] on the drop evaporation process. Depending on the surface wettability and surface structure, droplets evaporate in different modes. The widely accepted evaporation mechanisms, depending on the dynamics of the triple contact line (TCL), are the constant contact angle (CCA) mode, the constant contact radius (CCR) mode, and the CCR-CCA mixed mode [13,14]. Typically, the CCA mode happens on smooth hydrophobic substrates where the droplet contact line recedes while the contact angle remains constant to account for the liquid evaporated. On a hydrophilic and/or on a rougher substrate where the surface hysteresis is high though, the triple contact line tends to be pinned while the contact angle decreases with time, namely, the CCR mode. In addition, during evaporation of nanofluid droplets [15,16] or pure fluid droplets on structured surfaces [17], a stick-slip evaporative behavior has also been reported. As a consequence of the different evaporation behavior, the lifetime of a droplet is found to differ [9,18,19]. The evolution, and in particular, the lifetimes, of droplets evaporating in a variety of different modes of evaporation have been studied by Stauber *et el*. [20,21] and Schofield *et al*. [22] using the diffusion-limited evaporation model (see, for example, Popov [18] and Saada *et al*. [23]).

On the other hand, liquid desiccants are a special type of aqueous salt solution, which have excellent hygroscopic properties. Due to the hygroscopic nature of liquid desiccants, they are widely

applied in all kinds of dehumidification systems [24], absorption heat pumps [25,26], and absorption

heat transformers [27]. Most commonly used ionic liquid desiccant salts include lithium bromide

(LiBr), lithium chloride (LiCl) and calcium chloride (CaCl$_2$) [28]. These salts have strong affinity

and adhesion to the water molecules, and after dissolving in water, they reduce greatly the partial

vapor pressure of the solution at the liquid-air interface. In the case of droplet evaporation, the vapor

diffusion is driven by the vapor pressure difference between the saturated droplet interface and the

unsaturated air bulk [29]. Nonetheless, when it comes to liquid desiccant droplets, the vapor pressure

at the droplet interface becomes lower than the partial vapor pressure of the ambient air. Therefore,

the direction of vapor diffusion converses, and water vapor diffuses spontaneously from the air side

to the droplet side.

The coupled heat and mass transfer between humid air and liquid desiccant is fundamental and

of significant importance to all kinds of dehumidification applications. Up to now, most of the

research carried out on liquid desiccants addresses: the performance of dehumidifiers with different

flow patterns [30,31], different type of inner packing [32,33], presence or absence of inner heat

sources [34,35], and different desiccant solutions or ambient conditions [36,37], at the macro-scale or

at the system scale. Some theoretical models [38] have also been mathematically developed and

experimentally verified, which are capable of predicting to some extent the heat and mass transfer

process within the dehumidifier as a whole system. Despite of the above mentioned studies, the

performance of liquid desiccant droplets within a dehumidifier has been rarely reported. At the inlet

of the dehumidifier, desiccant droplets are formed at the liquid distributor before impinging onto the

inner packing [39]. Upon impingement, discrete drops varying in size and shape appear at the top of

the packing and flow down in a dropwise or filmwise fashion depending on the surface wettability. In

75 industrial applications, the inner fillers vary from light polymers, non-corrosive ceramics, to

76 high-strength metals [40], which provide different surface wettability, and therefore the flow regime

77 of the desiccant solution inside also differs. A further investigation on vapor absorption into

78 individual liquid desiccant droplets will shed light on the absorption process especially at the initial

79 stage of dehumidification where droplets form and exhibit an initial contact with the substrate.

80 Further understanding on the dynamics of droplet growth during vapor absorption on different

81 substrates will also help providing new insights on the mechanisms of filmwise or dropwise

82 formation and its relation with surface properties, so that one can provide a more accurate prediction

83 of the vapor uptake happening inside different desiccant dehumidification devices.

84   Hence, in this study, we investigate the vapor absorption mechanisms of $LiBr-H_2O$ droplets on

85 surfaces with different wettability at certain controlled ambient conditions. Experiments are carried

86 out with 54 wt.% aqueous lithium bromide-water ($LiBr-H_2O$) droplets on hydrophobic

87 polytetrafluoroethylene (PTFE) and on hydrophilic glass substrates commonly used as inner packing

88 in dehumidification systems at laboratory and at industrial scales. The dynamics of triple contact line

89 (TCL) and the evolution of droplet volume are compared, indicating the strong effect of surface

90 wettability on the vapor absorption process into droplets. By looking into the solute diffusion process

91 on the droplet side we demonstrate the different kinetics of absorption and droplet growth function of

92 surface wettability. Moreover, several plausible explanations are provided to account for the apparent

93 droplet spreading phenomenon observed on hydrophilic glass substrates when compared to

94 hydrophobic PTFE one.

2. EXPERIMENTAL SETUP

95

96   Experiments are carried out within an insulated environmentally controlled chamber (800L,

97   PR-3KT from ESPEC Corp., Japan), capable of providing constant temperature, T_{amb}, and relative

98   humidity, RH (T_{amb} = -20 ℃ ~ 100 ℃ and RH = 20% ~ 98%) environments. In this study, experiments

99   are carried out at six representative ambient conditions with T_{amb} = 25 ℃ and 45 ℃, and RH = 30%,

100   60%, and 90%. During experimental observations, the environmental condition within the chamber is

101   monitored both by the chamber panel and by an electronic hygrothermograph (testo 610 from testo

102   AG (Germany), T_{amb} = -10 ℃ ~ 80 ℃ and RH = 20% ~ 100%). Schematic of the experimental setup is

103   shown in Figure 1, which includes: environmental chamber, CCD camera and lens, LED back light,

104   stainless steel laboratory jack, droplet dosing system and data acquisition system. The high-definition

105   CCD camera (Sentech STC-MC152USB with a RICOH lens and 25-mm spacing ring) along with a

106   LED backlight are used to image the droplet profile at 4.8 frames per second. The real-time video of

107   the droplet profile is thereafter processed with the software ImageJ[®] and MATLAB[®]. Then, the

108   evolutions of droplet volume, V (μL), contact radius, R (mm), and contact angle, θ (deg), along with

109   time, t (s), are extracted by assuming the shape of the droplet as spherical cap geometry.
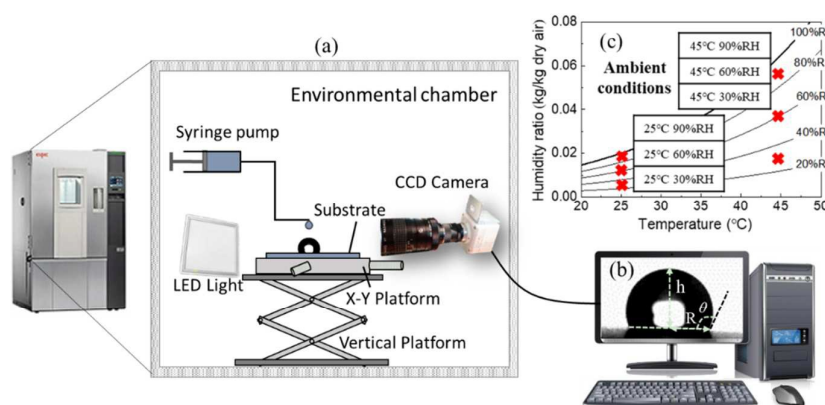

110
111   Figure 1   Overview of the experimental setup. (a) Experimental part: environmental chamber, CCD camera, back
112   light, stainless steel vertical platform, X-Y platform, droplet dosing system; (b) data acquisition system with
113   Image J[®] and Matlab[®]; (c) Experimental conditions shown on the psychrometric chart.

114   54.0 wt.% lithium bromide (LiBr) solution and deionized water from Sigma-Aldrich are used as

115   testing fluids for the experimental observations. Typically, a sessile droplet whose largest dimension

116   is smaller than the capillary length will adopt spherical cap shape. For pure water in air, the capillary

117   length is estimated as 2.6 ~ 2.7 mm (calculated according to the definition of capillary length,

118    $\lambda = \sqrt{\gamma_{lg}/\rho g}$ [41], where λ is the capillary length in meters, γ_{lg} is the liquid-air surface tension

119   in N/m, ρ is the liquid density in kg/m^3, g is the gravitational acceleration in m^2/s). On the other

120   hand, for 54 wt.% LiBr- H$_2$O solution in air, the capillary length is ca. 2.42 mm. In our study, the

121   contact radius of both water droplets and LiBr-H$_2$O droplets did not exceed the capillary length

122   throughout the vapor absorption process, therefore, the gravity effect on the droplet shape can be

123   neglected and the assumption of treating the droplet as spherical cap is reasonable. We note here that

124   some vapor absorption onto the droplet might happen during droplet deposition.

125   Table 1 includes the properties of 54.0 wt.% LiBr-H$_2$O solution and those of pure water.

126   LiBr-H$_2$O solution has higher viscosity and greater liquid-gas surface tension, which contributes to

127   the higher equilibrium contact angle of LiBr-H$_2$O droplets on the same substrates when compared to

128   pure water droplets. Moreover, the boiling point of 54 wt.% LiBr-H$_2$O solution at 1 atmosphere is ca.

129   40 ℃ higher than that of pure water, which suggests the apparent lower vapor pressure at the solution

130   surface.

131   Table 1   Properties of 54% wt. LiBr solution and distilled water as specific heat capacity c_p (kJ/kg/K); density
132   ρ (kg/m^3); liquid-gas surface tension γ_{lg} (mN/m); viscosity v (mPa·s); thermal conductivity k (W/m/K);
133   boiling temperature $T_{boiling}$ (℃). Properties shown were obtained at 20 ℃ and at 1 atm.

Liquid type	c_p (kJ/kg/K)	ρ (kg/m^3)	γ_{lg} (mN/m)	v (mPa·s)	k (W/m/K)	$T_{boiling}$ (℃)
54% wt. LiBr solution	1.98	1600	91.54	4.751	0.4286	140
Distilled water	4.18	998	72.75	1.005	0.5984	100

134

135

Table 2   Properties of glass and PTFE substrates as density ρ (kg/m3); specific heat capacity c_p (J/kg/K); thermal conductivity k (W/m/K); thermal diffusivity α (m^2/s), $\alpha = k/\rho c_p$; surface roughness S_q (μm); and equilibrium contact angle for a 3 μL water droplet, $\theta_{0,W}$ (°), and for a 3 μL LiBr droplet, $\theta_{0,S}$ (°), at 20 ℃ and 1 atm.

Material	ρ (kg/m^3)	c_p (kJ/kg/K)	k (W/m/K)	α (m^2/s)	S_q (μm)	Equilibrium $\theta_{0,W}$ (°)	Equilibrium $\theta_{0,S}$ (°)
PTFE	2200	1.05	0.25	0.52	0.516	98° ± 3°	108° ± 3°
Glass	2400	0.84	0.75	2.15	0.012	70° ± 3°	75° ± 3°

140   Two types of substrates are chosen for the experiments; hydrophobic polytetrafluoroethylene

141   (PTFE) and hydrophilic glass. Table 2 lists the main properties of the two substrates, where the

142   surface roughness, S_q, is assessed with a 3D optical laser scanning microscope (Olympus LEXT

143   OLS4000, Japan), and the droplet equilibrium contact angle for deionized water, θ_0, is measured

144   using a custom-built contact angle analyzer at laboratory ambient conditions, *i.e.*, T_{amb} = 20 °C and

145   55% *RH*.

146   Before experiments, substrates are cleaned by immersing each sample in an ultrasonic bath with

147   ethanol for 15 minutes. After that, the sample is taken out and rinsed with large amount of deionized

148   water. Then, substrates are further dried with filtered compressed air to remove any possible

149   remaining dust or contaminants. After drying, the substrate is placed inside the chamber for

150   sufficiently long time for the substrate to reach equilibrium temperature with the environment. Then,

151   a droplet of 4 ± 0.5 μL is deposited within the environmental chamber on the chosen substrate. We

152   note here that dosing system and substrate are inside the chamber for sufficient time to ensure that

153   both fluid and substrate are at T_{amb}. Before droplet deposition, CCD acquisition is started and the

154   evolution of the droplet profile is then recorded in time.

155

3. EXPERIMENTAL RESULTS

3.1. Droplet TCL dynamics on hydrophilic glass substrates

Representative evolution curves of contact angle, θ, and normalized contact radius, R/R_0, of LiBr-H_2O droplets on a hydrophilic glass substrate for the six different ambient conditions are plotted in Figure 2. The initial contact angle for LiBr-H_2O droplets on a glass substrate is *ca.* 75° ± 3°, about 5° larger than that of pure water droplets due to the higher liquid-air surface tension (see Table 1). Depending on the ambient condition, droplets on hydrophilic glass substrates show different degree of spreading. We note here that the slow spreading evolution reported here differs from early regimes spreading where the droplet establishes the spherical cap in the first few seconds after deposition. Further discussion on the spreading mechanisms is included within Section 4.2. At 30% *RH* (Figure 2(a)), θ decreases from 75° to about 52°, while the contact radius increases to 1.24 times of its initial value. At 60% *RH* (Figure 2(b)) and at 90% *RH* (Figure 2(c)), qualitatively, the decrease in contact angle follows the same trend to that reported for 30% *RH*, where there is an initial decrease and then flattens. Quantitatively, at high humidity of 90% *RH*, the contact angle decreases to about 40° while the contact radius increases to ca. 2 times due to greater drop spreading coupled with greater amount of water vapor absorbed. The quantitative behavior at intermediate humidity of 60% *RH* (Figure 2(b)) is found to lie between low and high relative humidity cases where the contact angle decreases to a value between 40° and 50° and the contact radius increases to a value of ca. 1.4 times the initial one. Ambient temperature T_{amb} is found to influence the rate of droplet spreading during the initial stage of vapor absorption, where the droplet contact angle and contact radius vary more rapidly at 45 ℃ than at 25 ℃.
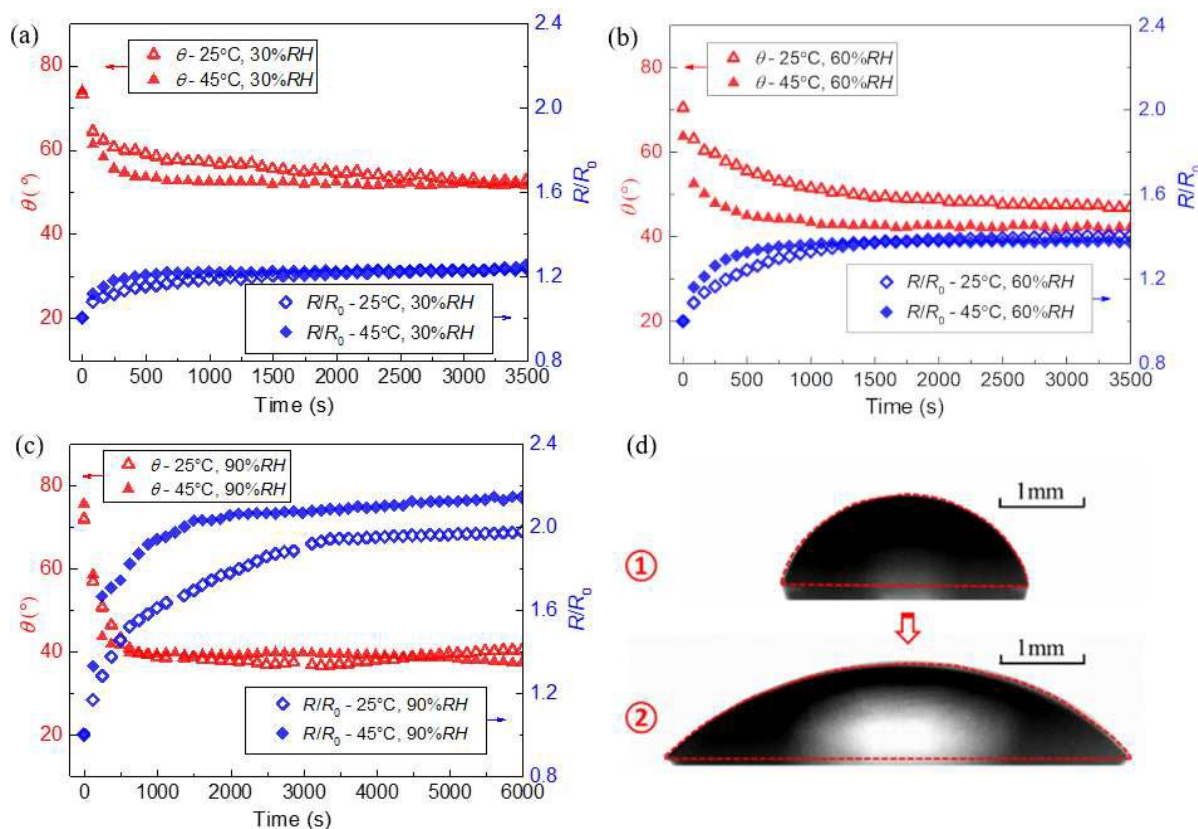
177

Figure 2   Evolution of (up-triangles) contact angle, θ (°), and (diamonds) normalized contact radius, R/R_0, of
LiBr-H$_2$O droplets, versus time (s) for (a) 30% RH, (b) 60% RH, and (c) 90% RH, at (open symbols) T_{amb} =
25 ℃ and (close symbols) T_{amb} = 45 ℃ on hydrophilic glass substrates. (d) Initial (t = 0 s) and final (t = 6000 s)
snapshots of a LiBr-H$_2$O droplet on a hydrophilic glass substrate at 45 ℃ and 90% RH.

182   To exemplify the droplet profile change during vapor absorption, Figure 2(d) shows snapshots of

183   a LiBr-H$_2$O droplet on a hydrophilic glass substrate at 45 ℃ and 90% RH at the initial (t = 0 s) and at

184   the final (t = 6000 s) stage of absorption. Due to water uptake, an expansion of droplet volume is

185   observed. In addition, due to both droplet expansion and contact angle decrease, the triple contact

186   line (TCL) advances greatly throughout the absorption process, $i.e.$, radius increases to

187   approximately 1.2, 1.4 and 2.0 times its initial value at 30%, 60% and 90% RH, respectively.

188   **3.2. Droplet TCL dynamics on hydrophobic PTFE substrates**

189   Representative evolution curves of contact angle, θ, and normalized contact radius, R/R_0, of

190   LiBr-H_2O droplets on a hydrophobic PTFE substrate for the six different ambient conditions are

191   shown in Figure 3. The initial contact angle of a LiBr-H_2O droplet on the hydrophobic PTFE

192   substrate is *ca.* $108° ± 3°$ for all the experimental conditions, about $10°$ higher than that of pure water

193   droplets on the same PTFE substrate studied. At 30% *RH* (Figure 3(a)) the contact angle of a

194   LiBr-H_2O droplet decreases from $108°$ to $93° ± 4°$, while the contact radius increases to ca. 1.2 times

195   its initial value and reaches equilibrium after *ca.* 700 seconds. At 60% *RH* (Figure 3(b)) the droplet

196   contact radius increases to 1.3 times its initial value, while the droplet contact angle decreases from

197    $108°$ to $93°$. At 90% *RH* (Figure 3(c)) the droplet grows even larger as the final R/R_0 reaches *ca.* 1.6,

198   while the contact angle decreases from $107°$ to $90°$. Spreading behavior reported here also differs

199   from early regime spreading where the droplet establishes the spherical cap, which is further

200   discussed within Section 4.2. For the same ambient humidity, the increase in contact radius and the

201   decrease in contact angle are actually more marked at high ambient temperatures (T_{amb} = 45 ℃) than

202   at low ambient temperatures (T_{amb} = 25 ℃).

203   Moreover, on a PTFE substrate we report the sudden decrease in the contact angle accompanied with

204   the increase in the contact radius in an advancing stick-slip fashion, which is marked with black

205   arrows in Figure 3(b) and Figure 3(c). We henceforth refer to such behavior as advancing stick-slip.

206   For a LiBr-H2O droplet sitting on a hydrophobic PTFE substrate, the TCL remains pinned or slightly

207   increases while the contact angle increases to account for the increase in volume due to vapor

208   absorption (Figure 3(b) and Figure 3(c)). Heterogeneities on the PTFE solid surface may induce the

209   observed additional pinning barrier, which must be overcome before the TCL slips or jumps forward

210   [15, 16]. Typically, as the contact angle deviates from the equilibrium one, the droplet gains certain

211   excess of free energy and when such excess of free energy overcomes the pinning barrier exerted by

212 the solid surface the jump of the TCL ensues [16]. The advancing slip or jump of the TCL observed

213 is characterized by the sudden decrease in the contact angle and the associated increase in the contact

214 radius. Advancing stick-slip reported here differs from receding stick-slip behavior reported earlier

215 during nanofluid droplet evaporation [15, 16] or pure fluid droplets evaporating on structured

216 surfaces [17]. In the case of receding stick-slip, the contact angle decreases to account for the loss of

217 volume due to evaporation while the TCL remains pinned to the substrate [15, 16]. Then, as the

218 droplet evaporates, the excess of free energy increases and when the excess of free energy becomes

219 greater than the pinning barrier the jump of the TCL ensues [16]. During receding stick-slip the jump

220 of the TCL is characterized by the sudden increase in the contact angle and the associated decrease in

221 contact radius.   In addition, the advancing stick-slip appears to be more frequent and marked at high

222 humidity conditions; especially at 90% *RH* (Figure 3(c)), due to the more rapid droplet expansion

223 when compared to 30% *RH* (Figure 3(a)) and to 60% *RH* (Figure 3(b)). To illustrate the vapor

224 absorption behavior, Figure 3(d) shows snapshots of a LiBr-H2O droplet on a hydrophobic PTFE

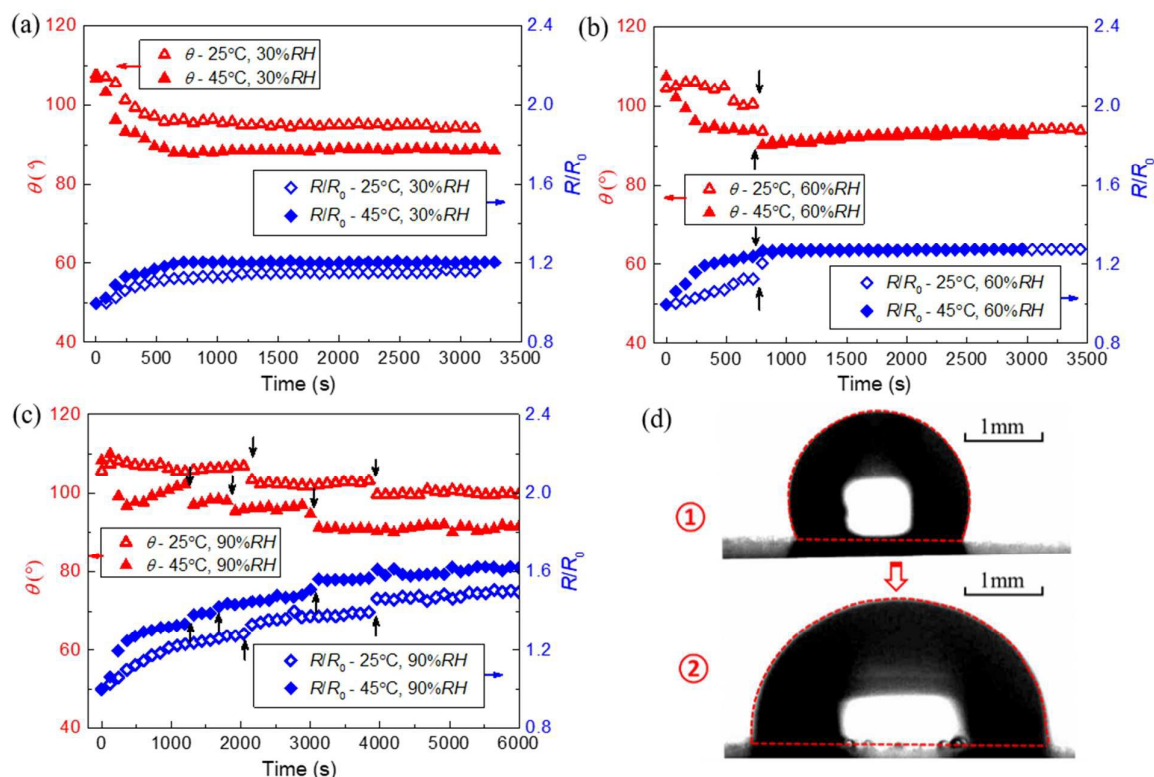225 substrate at 45 °C and 90% *RH* at initial droplet deposition (*t* = 0 s) and at later stage of absorption (*t*

226 = 6000 s).

Figure 3   Evolution of (up-triangles) contact angle, θ, and (diamonds) normalized contact radius, R/R_0, of LiBr-H_2O droplets, versus time (s) for (a) 30% RH, (b) 60% RH, and (c) 90% RH, at (open symbols) T_{amb} = 25 ℃ and (close symbols) T_{amb} = 45 ℃ on a hydrophobic PTFE substrate. (d) Initial (t = 0 s) and final (t = 6000 s) snapshots of a LiBr-H_2O droplet on PTFE substrate at 45 ℃ and 90% RH.

It is then evident that hygroscopic LiBr-H_2O droplets behave differently depending on the wettability of the surface. The characteristic behavior of absorption for LiBr-H_2O droplets on a hydrophobic PTFE substrate is then characterized by smaller TCL spreading when compared to that observed on hydrophilic glass. On a PTFE substrate the increase of both droplet contact radius and droplet height are solely due to vapor absorption, whereas for LiBr-H_2O droplets on a hydrophilic glass, the coupling mechanisms of both droplet spreading and vapor absorption govern the advancing behavior of the TCL and its dynamics. We also note here that the dynamics of the TCL during vapor absorption into liquid desiccant droplets differ from those of droplet evaporation, droplet condensation, droplet growth upon freezing and/or from the simultaneous monotonic increase in

241   contact angle and decrease in contact radius due to the water adsorption-absorption and/or

242   condensation during organic solvent evaporation [42-45].

243   **3.3. Evolution of droplet volume during vapor absorption**

244   During vapor absorption, the droplet volume increases in different trends depending on the

245   ambient condition. Figure 4 presents evolution of the normalized droplet volume along with time on

246   hydrophilic glass (Figure 4(a)) and on hydrophobic PTFE substrates (Figure 4(b)). At low ambient

247   humidity of 30% *RH*, the droplet volume increases ca. 10%, and reach equilibrium with the ambient

248   after several hundred seconds. At 60% *RH*, droplets expand more apparently, and it also takes longer

249   for the droplets to reach equilibrium with the ambient, *ca.*1000 ~ 2000 seconds. At high humidity of

250   90% *RH*, droplets grow following a saturating trend throughout the complete duration of the

251   experimental observations ca. 2 hours. When comparing the final values of the droplet volume in

252   Figure 4, it shows that the final expansion ratio of droplet volume, V_f/V_0, is only related to the

253   relative humidity: V_f/V_0 (30% *RH*) ≈ 1.07, V_f/V_0 (60% *RH*) ≈ 1.5 and V_f/V_0 (90% *RH*) ≈ 2.7 ~ 3.3

254   regardless of surface wettability and ambient temperature. We note here that although surface

255   wettability does not have an impact on the final droplet volume, there are differences on the

256   absorption kinetics, which will be discussed in the next Section (Section 4).
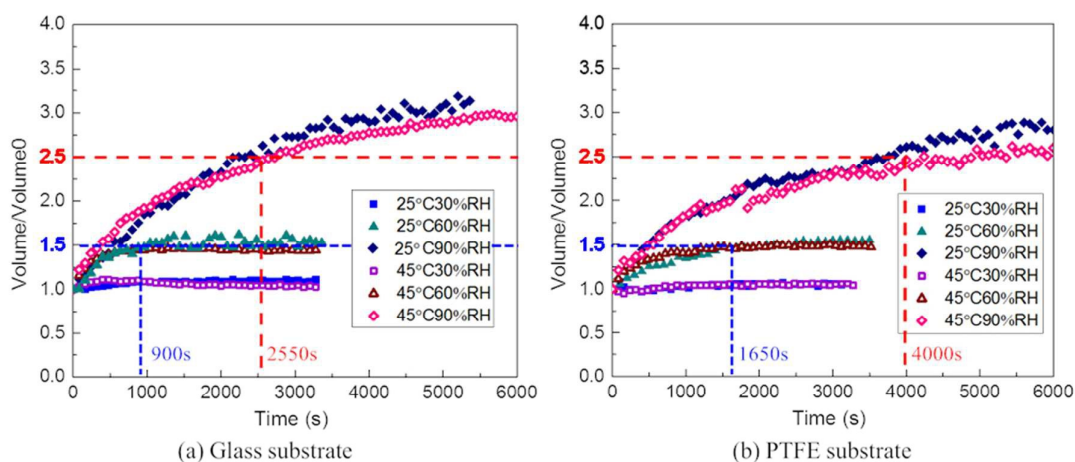
257

Physical Chemistry Chemical Physics Accepted Manuscript

Figure 4   Evolution of normalized droplet volume, V/V_0, versus time, t (s), for LiBr-H_2O droplets on (a) glass substrate and (b) PTFE substrate at (close symbols) $T_{amb} = 25$ ℃ and (open symbols) $T_{amb} = 45$ ℃ for (squares) 30%, (up-triangles) 60% and (diamonds) 90% RH. (Blue dashed line) time at which the droplet reaches $V/V_0 = 1.5$ at 60% RH and (red dashed line) time at which the droplet reaches $V/V_0 = 2.5$ at 90% RH, on a glass and on a PTFE substrate.

As marked with red and blue dashed lines in Figure 4, for the same ambient condition of 45 ℃ and 90% RH, on a hydrophobic PTFE substrate it takes 4000 seconds for the LiBr-H_2O droplet to expand to 2.5 times of its initial volume, while on a hydrophilic glass substrate it takes *ca.* 2550 seconds. At 45 ℃ and 60% RH, on a hydrophobic PTFE substrate it takes 1650 seconds for the droplets to expand to 1.5 times of its initial volume, while on a hydrophilic glass substrate it takes about half of it, *i.e.*, *ca.* 900 seconds. To provide further quantification and comparison on the amount of water uptake during the absorption process, Table 3 presents the normalized droplet volume at different instants of time with $t = 0$ s as the droplet deposition. On one hand, at low relative humidity 30% RH the droplet volume remains constant during the absorption times reported in Table 3. On the other hand, when looking into medium and high relative humidity conditions, i.e., 60% RH and 90% RH, the droplet volume increases faster on hydrophilic glass when compared to hydrophobic PTFE. We note here that in the case of high relative humidity 90% RH, the droplet volume continuously increases for the experimental times reported.

277　　Table 3　　Normalized droplet volume, V/V_0, at 25 °C and 30%, 60% and 90% *RH* on both hydrophilic glass and

278　　　　hydrophobic PTFE substrates at $t = 500, 1000, 2000, 3000$ and 4000 seconds with $t = 0$ seconds as the droplet

279　　　　　　　　　　　　　　　deposition instant.

Normalized droplet volume, V/V_0, at 25 ℃	500 s		1000 s		2000 s		3000 s		4000 s	
	glass	PTFE	glass	PTFE	glass	PTFE	glass	PTFE	glass	PTFE
30% *RH*	1.06	1.09	1.09	1.09	1.10	1.11	1.11	1.11	-	-
60% *RH*	1.32	1.33	1.55	1.48	1.60	1.57	1.61	1.63	-	-
90% *RH*	1.49	1.46	1.82	1.75	2.33	2.16	2.73	2.39	2.89	2.52

280　　　　To demonstrate the amount of water absorbed during droplet expansion depending on T_{amb} and

281　　*RH*, Figure 5 includes the psychometric chart representing the humidity ratio (kg water/ kg dry air)

282　　versus T_{amb} and *RH*. The properties of LiBr-H_2O solution and humid air in the chart are calculated

283　　with embedded functions in EES[®] (Engineering Equation Solver) software. Black solid lines in

284　　Figure 5 show the condition (T_{amb} and humidity ratio) of ambient air at different *RH*, while blue

285　　dashed lines represent the condition (T_{amb} and humidity ratio) of the equivalent humid air layer at the

286　　surface of LiBr-H_2O solution with different concentrations. It can be seen that the iso-concentration

287　　curves of LiBr-H_2O solution and the iso-relative humidity curves of ambient air are in parallel or

288　　overlap with each other, which indicates that the humid air at a certain relative humidity is in

289　　equilibrium with the solution for a certain salt concentration. When the ambient relative humidity

290　　keeps constant, the desiccant droplet will keep absorbing water vapor until it reaches equilibrium
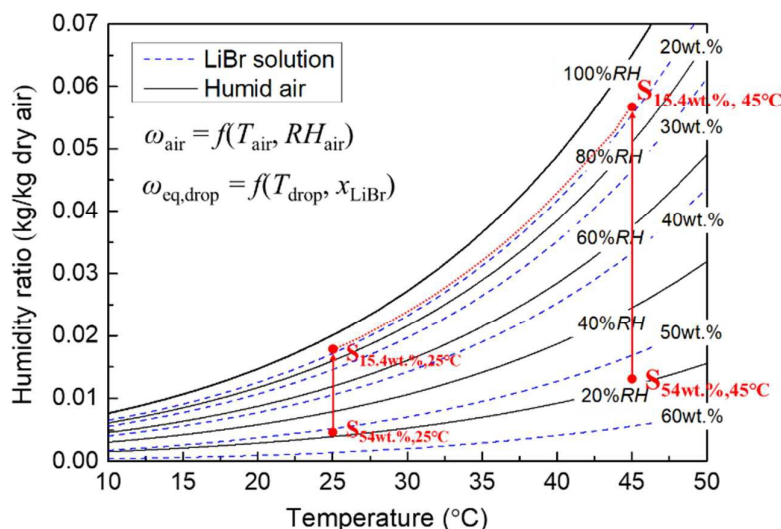
291　　with the ambient.

292

293   Figure 5   Psychrometric chart showing the condition of the humid air (solid line) at different relative humidity, and

294   the condition of equivalent humid air layer at the surface of LiBr-H$_2$O solution (blue dashed line) at different

295   concentrations. Red solid arrows present the concentration variation of LiBr-H$_2$O solution during vapor

296   absorption.

297   The red points in Figure 5 represent the initial and final conditions($S_{initial,25℃}$, $S_{final,25℃}$, $S_{initial,45℃}$,

298 $S_{final,45℃}$) of the LiBr-H$_2$O droplets at 25 ℃, 45 ℃, and 90% RH. During vapor absorption, the liquid

299 desiccant salts stay within the droplet in the form of ions, and therefore, the solution concentration of

300 LiBr, x, should follow the solute conservation equation shown in Eq. (1):

$$\rho_{initial}V_{initial}x_{initial} = \rho_{final}V_{final}x_{final} \tag{1}$$

301   For droplets at 25 ℃ and 45 ℃, the expansion ratio of droplet volume is therefore derived as:

$$\left(\frac{V_{final}}{V_{initial}}\right)_{25°C} = \left(\frac{x_{initial}}{x_{final}}\right)_{25°C}\left(\frac{\rho_{initial}}{\rho_{final}}\right)_{25°C}, \quad \left(\frac{V_{final}}{V_{initial}}\right)_{45°C} = \left(\frac{x_{initial}}{x_{final}}\right)_{45°C}\left(\frac{\rho_{initial}}{\rho_{final}}\right)_{45°C} \tag{2}$$

302   Taking 90% RH as an example, the $\rho_{initial}/\rho_{final}$ is 1.430 at 25 ℃, and 1.433 at 45 ℃ according to

303 our calculation based on the correlation provided in Ref. [46]. And since the ratio of droplet

304 concentration $x_{initial}/x_{final}$ is also the same for 25 ℃ and for 45 ℃, the same final expansion ratio of

305 droplet volume $V_{final}/V_{initial}$ regardless of the ambient temperature and surface wettability is then

306 demonstrated.

307 **4. ANALYSIS AND DISCUSSION**

308 **4.1. Effect of surface wettability on the absorption kinetics**

309 From the evolution of droplet volume, it is also worth noticing that the surface wettability has a

310 strong effect on the kinetics of vapor absorption and on the dynamics of the TCL, which in turn

311 dictates the mechanisms of droplet growth. Further quantification of the results presented in Section

312 3 is included in Table 4, which shows the normalized vapor absorption rates for the first 100 seconds

313 after the droplet deposition. Droplets on hydrophilic glass substrates show higher vapor absorption

314 rates than those on hydrophobic PTFE. In addition, the expected greater initial absorption rates at

315 high ambient temperature (T_{amb} = 45 °C) when compared to low ambient temperature (T_{amb} = 25 °C)

316 are also highlighted.

317 Table 3   Normalized initial vapor absorption rate, $d(V/V_0)/dt$, during the first 100 seconds for: 25℃ - 60%
318   *RH*, 25℃ - 90% *RH*, 45℃ - 60% *RH*, and 45℃ - 90% *RH*, on hydrophilic glass and hydrophobic PTFE
319   substrates.

Normalized absorption rate $d(V/V_0)/dt$ (s^{-1})	25℃ - 60%*RH*	25℃ - 90%*RH*	45℃ - 60%*RH*	45℃ - 90%*RH*
Hydrophilic glass	0.00102	0.00103	0.00137	0.00132
Hydrophobic PTFE	0.00098	0.00089	0.00133	0.00124

320 Droplet growth due to vapor uptake into liquid desiccant droplets reported in this study is driven

321 by the vapor pressure difference between the humid air and the droplet surface. The vapor absorption

322 from the humid air into the LiBr-H_2O droplet can be divided into three steps: the water vapor

323 diffusion on the air side, the vapor to water phase-change transition at the air-liquid interface, and the

324 diffusion of water molecules from the droplet interface toward the droplet bulk (or the solute (Li^+,

325 Br^-) diffusion from the bulk of the droplet towards the droplet interface). Figure 6 shows

326 one-dimensional evolution of ambient air and liquid desiccant solution during the vapor absorption

327   process, where the thickness of the liquid layer for the diffusion of the solute equals the droplet

328   characteristic length (h^*), and the air layer is assumed to be infinite since the chamber is large

329   enough compared to the size of the droplets. At the very initial stage, right after the droplet

330   deposition ($t = 0$ seconds), we assume that there is no mass diffusion between the humid air and the

331   aqueous solution, and an apparent vapor pressure difference between the ambient air and the liquid

332   surface is present. Then, driven by the pressure difference, water vapor gradually diffuses from the

333   air side to the liquid-air interface, and gets absorbed. Due to vapor absorption, the concentration of

334   solute (Li^+ and Br^- ions) near the liquid-air interface decreases. Then, Li^+ and Br^- ions diffuse from

335   the high concentration side at the droplet bulk to the low concentration side at the liquid interface

336   following the concentration gradient. As the absorption process continues and as a consequence of

337   the increase in water concentration within the droplet, the vapor pressure difference between the

338   liquid surface and the ambient air decreases. At the same time, the concentration gradient of LiBr

339   solute within the aqueous solution also decreases until equilibrium is attained. The local change in

340   concentration at the liquid-air interface and in the droplet profile due to vapor absorption reported

341   here, differs from the concentration change due to preferential evaporation of one component during

342   evaporation of binary mixtures [43, 47-49].
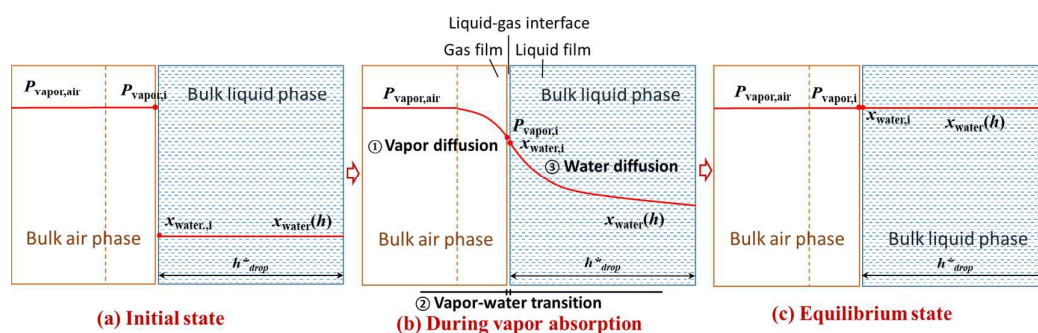

343

344   Figure 6   Schematic of water vapor concentration in the air side and the concentration of liquid water in the bulk of

345   the droplet (a) at initial stage right after droplet deposition, $t = 0$ s, (b) during vapor absorption, and (c) at

346   equilibrium, $t = \infty$.

347   Since vapor absorption is a surface area related problem, it is noteworthy providing a

348   comparison between the spherical cap surface area of liquid desiccant droplets on hydrophilic *versus*

349   hydrophobic substrates. For droplets on hydrophilic glass substrate, the interfacial area for mass

350   transfer is *ca.* 9.02~10.65 mm^2, while for droplets on hydrophobic PTFE, the interfacial area is *ca.*

351   9.04~10.68 mm^2. Since there is no large difference in the effective droplet areas for vapor absorption,

352   the absorption rate must be governed by the mass diffusion process on the air side and/or on the

353   liquid side. Typically, the mass diffusion rate in the liquid phase is $10^3 \sim 10^4$ times of that in the gas

354   phase ($D_{\text{water/air}}/D_{\text{LiBr/LiBr}-\text{H}_2\text{O}} \sim 10^{-5}/10^{-9} \sim 10^4$) [50]. Therefore, we can assume that the vapor

355   absorption process is limited by the solute diffusion on the liquid side.

356   The solute diffusion process within the LiBr-H$_2$O droplet can be further evaluated by the

357   characteristic time, τ, presented as Eq. (3),

$$\tau = L^2/D \tag{3}$$

358   where L is the characteristic length for mass diffusion, which we assume as the characteristic length

359   of the droplet, h^*, and D is the mass diffusion rate (m^2/s).

360   According to eq. (3), the characteristic time for the solute diffusion on the liquid side is

361   calculated as ca. 10^3 seconds, where the characteristic length of the droplet, L, is estimated as 1 mm,

362   and the water diffusion rate, D_s, is 10^{-9} m^2/s [51, 52]. It shows that the characteristic time for solute

363   diffusion is in the same order of magnitude to that of the vapor absorption period reported in the

364   experiments (500 ~ 8000 seconds). Hence, solute concentration gradient within the LiBr-H$_2$O droplet

365   is the dominant mechanism governing vapor absorption onto liquid desiccant droplets and cannot be

366   neglected.

367   Considering the solute diffusion process within the droplet governed by Fick's law, the

368 characteristic length for solute diffusion is the shortest path for the diffusing molecules of water to

369 reach the solid surface and for the Li^+ and Br^- molecules to reach the liquid-air interface, or to "meet"

370 each other. While the solid surface can be treated as an impermeable boundary with zero mass flux,

371 the liquid-air interface must be treated as a moving boundary condition governed by the change in

372 droplet volume due to water vapor absorption. On hydrophilic glass substrates where the droplet

373 contact angle is less than 90°, the characteristic length for solute diffusion required for the theoretical

374 description of this process is the droplet height $h^* = h_{drop}$ as shown in Figure 7(a). Whereas on

375 hydrophobic PTFE substrates where the droplet contact angle is larger than 90°, the characteristic

376 length for solute diffusion is the radius of curvature $h^* = \kappa_{drop}$ as shown in Figure 7(b). Further work

377 is currently being sought on the theoretical modelling of the vapor absorption process.
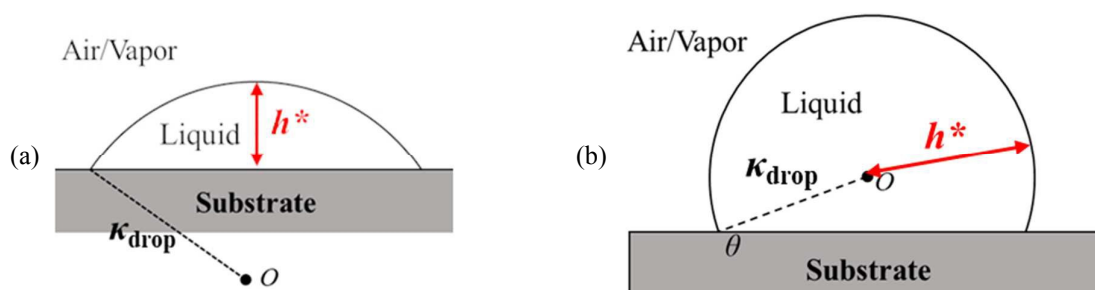
378 Figure 7 Characteristic droplet length, h^*, for solute diffusion within the LiBr-H_2O droplets (a) on hydrophilic
379 glass substrate, and (b) on hydrophobic PTFE substrates.

380   Figure 8 shows the evolution of the characteristic lengths for droplets on a hydrophilic glass

381 substrate and on a hydrophobic PTFE substrate in time at 45 ℃ and 60% RH (Figure 8(a)) and at 45 ℃

382 and 90% RH (Figure 8(b)). It shows that on glass substrates the characteristic length (droplet height)

383 decreases along with time at 60% RH as a consequence of the reported droplet spreading. While at

384 90% RH the characteristic length actually increases due to the greater amount of absorbed water

385 vapor when compared to 60% RH. By comparison, on PTFE substrates the characteristic length

386   (radius of curvature) increases to greater extent when compared to the characteristic length reported

387   on hydrophilic glass substrates (Figure 8). At 60% *RH* the characteristic length increases from about

388   1.18 mm to about 1.4 mm in 3500 seconds, while at 90% *RH*, the characteristic length increases from

389   about 1.1 mm to about 1.7 mm in 7000 seconds.

390   The characteristic time τ for mass diffusion defined in Equation 3, accounts for how long it takes

391   for the water molecules to diffuse over the distance h^*, hence as h^* increases so does τ, and droplet

392   saturation is reached later on the hydrophobic case. At 45 ℃ and 60% *RH*, for the same diffusion

393   coefficient, $\tau_{\text{PTFE}}/\tau_{\text{glass}} \sim h^*_{PTFE}/h^*_{glass} \sim$ 1.96. This estimation remarkably agrees with the

394   experimental results where it takes 1650 seconds and 900 seconds for the droplets to reach

395   equilibrium on PTFE substrate and on glass substrate respectively, *i.e.*, τ_{PTFE} / τ_{glass} = 1650 / 900 $\sim$

396   1.83.
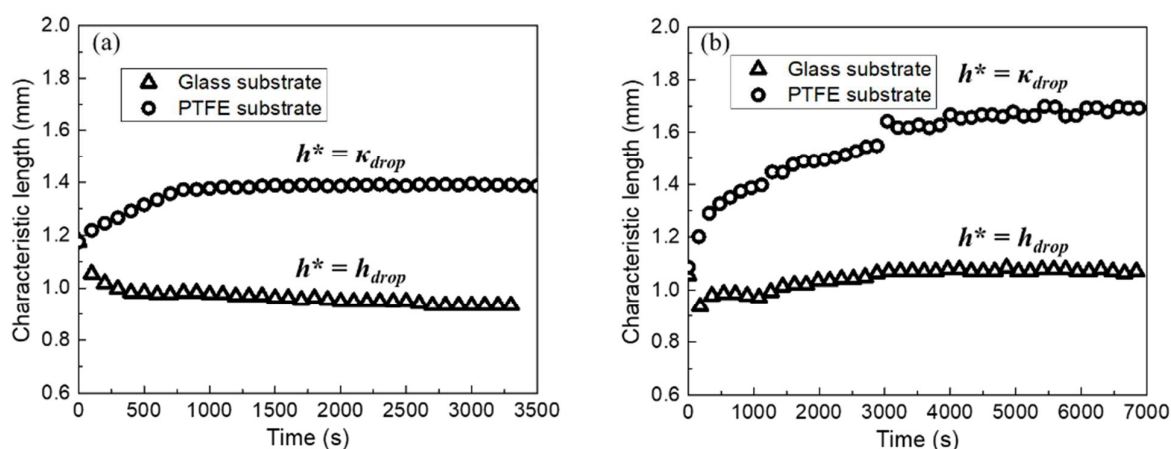
397   Figure 8 Evolution of characteristic lengths for solute diffusion within the LiBr-H₂O droplets, versus time (s), on
398   (triangles) hydrophilic glass substrates and on (circles) hydrophobic PTFE at (a) 45 ℃ and 60% *RH*, and at (b)
399   45 ℃ and 90% *RH*.

400   The above analysis clearly demonstrates that surface wettability has a strong impact on the

401   mechanisms of growth and spreading of hygroscopic lithium bromide desiccant droplets. Due to the

402   shorter characteristic length for solute diffusion, droplets on hydrophilic glass substrate show faster

403　vapor absorption rates. Since the efficiency and dehumidification capacity of packed towers are

404　closely related to the vapor absorption rate of the liquid desiccant, for industrial applications, we then

405　propose hydrophilic inner packing as the optimum configuration to further enhance the efficiency

406　and dehumidification capacity of such systems. .

4.2. Mechanisms of droplet spreading during vapor absorption
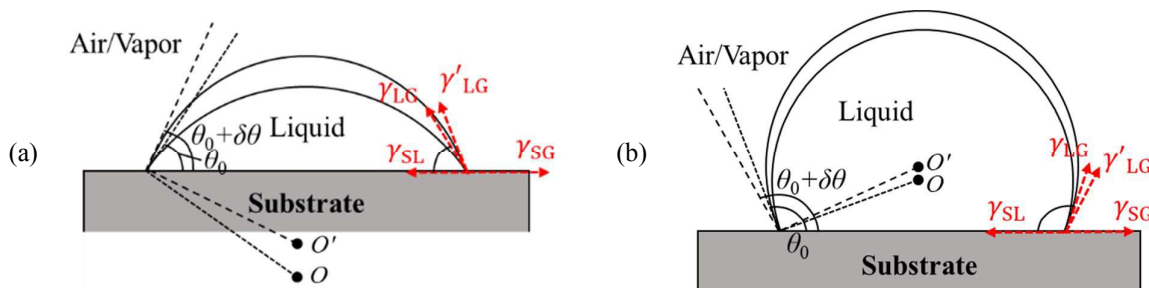
408　　　As described in Section 3, on hydrophilic glass substrates LiBr-H_2O droplets show a clear

409　spreading trend with monotonically increasing contact radius and decreasing contact angle (Figure 2),

410　while on hydrophobic PTFE substrates no apparent additional spreading is observed (Figure 3). We

411　note here that right after droplet deposition, there is a competition between capillary and viscous

412　dissipation forces occurring within the first instant after deposition prompting the spherical cap shape

413　of the droplet. This initial transient spreading differs from the timescales of spreading reported on

414　hydrophilic glass substrates upon vapor absorption. In previous literature, droplet spreading

415　phenomenon is reported in the droplet deposition process [53]. In those studies, the droplet spreading

416　is due to competition between capillary driving forces and viscous dissipation, and takes place within

417　the first seconds right after droplet deposition following Tanner's law [54]: $R(t) \propto t^{1/10}$. The time

418　scale of spreading is in the order of milliseconds for low viscosity liquids such as water in air on

419　boro-silicate glass substrates [53] or hexadecane on copper and/or glass [55]. However, in our work

420　LiBr-H_2O droplets spread along with a time scale ca. $10^2 \sim 10^3$ s greater than for early regimes of

421　spreading. Therefore, classical droplet spreading described by Tanner's law cannot be used to explain

422　the spreading of the TCL observed during vapor absorption on a hydrophilic substrate.

423　　　Next, to elucidate the different spreading behavior depending on the substrate wettability

424   reported in our study, we look into the different binary interactions at the TCL. Seemingly, to the

425   phenomena taking place during receding stick-slip earlier reported in literature, during vapor

426   absorption on a hydrophobic PTFE surface the TCL remains pinned to the surface because of the

427   intrinsic energy barrier presumably induced by substrate heterogeneities [16,56,57]. Then, the

428   contact angle increases to account for the increase in droplet volume. As the contact angle deviates

429   from that of equilibrium, the droplet gains certain excess of free energy [57,58]. As the excess of free

430   energy overcomes the intrinsic energy barrier induced by the solid substrate the jump or slip of the

431   contact line takes place [15, 16, 57, 58]. Next, we provide a qualitative local force balance at the TCL

432   for establishing the different nature of the intrinsic energy barrier depending on the wettability of the

433   surface, similar to the one proposed by Shanahan [16, 57, 58]. Figure 9 presents schematic of the

434   droplet profile at equilibrium contact angle, θ_0, and at slightly larger contact angle when respect to

435   the equilibrium one, $\theta_0+\delta\theta$, due to vapor absorption on (a) hydrophilic glass and (b) on hydrophobic

436   PTFE substrates. At the equilibrium state, the profile of a droplet on a smooth ideal surface follows

437   the balanced Young's equation, $\gamma_{SG} - \gamma_{SL} = \gamma_{LG}\cos\theta_0$, which accounts for the respective binary surface

438   tensions: solid-gas, γ_{SG}, solid-liquid, γ_{SL}, and liquid-gas, γ_{LG} [59]. As conveyed above, after the

439   deposition of a desiccant droplet on a substrate in the presence of a humid environment, the droplet

440   volume will increase due to vapor absorption. Within a finite short time, δt, and assuming the droplet

441   contact line as pinned, the contact angle will increase due to volume expansion to $(\theta_0+\delta\theta)$. Moreover,

442   since the solution near the droplet surface gets diluted due to water absorption, the liquid-gas surface

443   tension γ_{LG} will decrease by $\delta\gamma_{LG}$. Due to the variations in both the contact angle and the liquid-gas

444   surface tension, the force balance at the TCL is altered, and as a consequence an extra horizontal

445   force, δF, arises which tends to depin the contact line. By neglecting the second order small quantity,

446   δF can be derived as Eq. (4):

$$\delta F = \left(\gamma_{LG} - \delta\gamma_{LG}\right)\cos\left(\theta_0 + \delta\theta\right) - \gamma_{LG}\cos\theta_0 \approx -\gamma_{LG}\sin\theta_0\delta\theta - \delta\gamma_{LG}\cos\theta_0 \qquad (4)$$

447   Figure 9   Schematic of droplet profiles at the equilibrium state and at a slightly different contact angle when
448   compared to equilibrium one ($\theta_0 \rightarrow \theta_0 + \delta\theta$) due to vapor absorption on (a) hydrophilic glass substrate and on (b)
449   hydrophobic PTFE substrate.

450   On hydrophilic substrates, the droplet contact angle is smaller than 90°, and the value of $\cos\theta_0$ is

451 positive. In this case, the absolute value of the depinning force can be expressed as

452 $\left|\delta F\right|_{\theta<90°} = \left|\gamma_{LG}\sin\theta_0\delta\theta\right| + \left|\delta\gamma_{LG}\cos\theta_0\right|$. While on hydrophobic substrates, the contact angle is larger

453 than 90°, and the absolute value of the depinning force can be then expressed as

454 $\left|\delta F\right|_{\theta>90°} = \left|\gamma_{LG}\sin\theta_0\delta\theta\right| - \left|\delta\gamma_{LG}\cos\theta_0\right|$. Therefore, for the same change in the contact angle, the

455 depinning force is larger on hydrophilic substrates than on hydrophobic ones: $\left|\delta F\right|_{\theta<90°} > \left|\delta F\right|_{\theta>90°}$.

456 Then, for an identical intrinsic energy barrier, $\partial U/\partial r$, it is easier for the TCL to advance on

457 hydrophilic glass substrates.

458   Figure 10 shows the evolution of liquid-air surface tension, γ_{LG}, along with vapor absorption for

459 the six experimental conditions studied by assuming the solute distribution within the droplet as

460 homogenous [60]. Depending on the experimental condition investigated, γ_{LG} of LiBr-H_2O droplet

461 decreases as water vapor is absorbed. In addition, as for common fluids, at higher temperature,

462 LiBr-H_2O droplets have smaller surface tension than at low temperatures. Moreover, as absorption

463 takes place, the surface tension decreases with time and changes in surface tension are more marked

464   at higher ambient humidity conditions as shown in Figure 10. In the extreme case of 45 ℃ and 90%

465   RH, the surface tension decreases from ca. 88.04 mN/m to ca. 74.78 mN/m, which is still larger than

466   that of pure water droplet at 45 ℃ ($\gamma_{LG,water,45℃} \approx 69.14$mN/m [61]). The decrease in the droplet

467   surface tension partly accounts for the contact angle decrease during vapor absorption. Nevertheless,

468   the decrease in contact angle during vapor absorption is about 30°, which cannot be accounted for by

469   the contact angle change caused purely by the decrease in surface tension. Therefore, additional
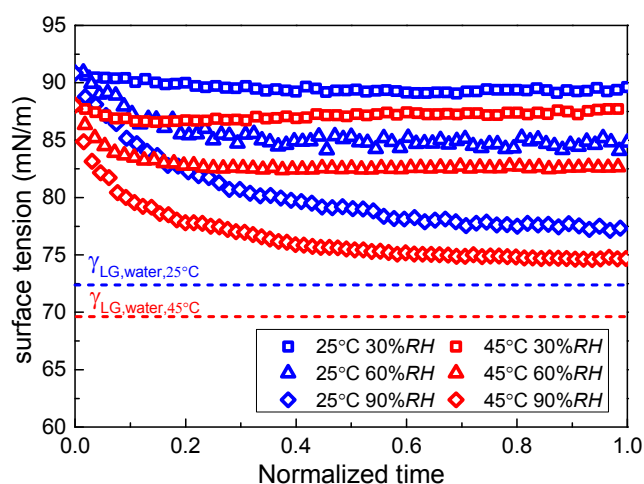
470   explanations are expected.

471

472   Figure 10 Evolution of surface tension of LiBr-H_2O droplets along with time during vapor absorption on a
473   hydrophilic glass substrate.

474   Compared to hydrophobic PTFE substrates, the hydrophilic nature of glass substrates induces

475   higher adhesion force to water molecules [62]. Therefore, in humid environments, water molecules

476   may accumulate near the glass surface due to adsorption [63]. In the presence of a LiBr-H_2O droplet,

477   the surface near the contact line will absorb more water vapor and induce both density gradient and

478   surface tension gradient along the droplet interface. In previous literature, droplet spreading has been

479   observed under surface tension gradients induced by localized surfactant addition [64], as well as by

480   an imposed temperature gradient [65]. Therefore, the density gradient and surface tension gradient

481   induced by non-uniform absorption across the droplet surface can be another plausible reason for the

482   droplet spreading observed in this study.

483   Furthermore, when looking into a moving contact line, a precursor film is usually considered to

484   be ahead of the visible droplet bulk [66-68]. In previous studies, the existence of precursor film has

485   been verified by advanced experimental techniques such as atomic force microscopy (AFM) [69],

486   and epifluorescence inverted microscopy [70], amongst others [71]. Figure 11 shows the proposed

487   schematic of the continuous transition from the macroscopic droplet profile to the microscopic

488   precursor film at the triple contact line for a spreading droplet on a hydrophilic substrate. The length

489   of the diffusive precursor film is proportional to the square root of time and can be expressed as Eq.

490   (5) [70].

$$L_p = \sqrt{\frac{A}{3\pi\eta h_c}} t^{1/2} \tag{5}$$

491   where L_p is the length of the precursor film, A is the effective Hamaker constant, η is viscosity, h_c is

492   the cutoff thickness, and t is time.

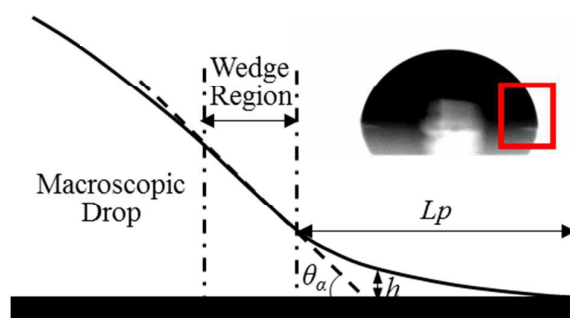493   Figure 11 Schematic of microscopic features in the vicinity of the advancing contact line on a hydrophilic substrate
494   as: precursor film ahead of the visible macroscopic droplet [70], wedge region and macroscopic droplet.
495   Macroscopic droplet profile is also included along.

496   For droplets on a hydrophobic PTFE substrate, due to the larger droplet curvature, the cutoff

497   thickness is larger than that of droplets on hydrophilic glass [72]. According to Eq. (5), the length of

498   the precursor film is inversely proportional to the square root of the cutoff thickness, hence the length

499   of precursor film will be. During experiments, vapor absorption happens both at the macroscopic

500   droplet interface and at the precursor film. As vapor absorption proceeds, the precursor film will

501   gradually grow thicker, with the inner side merging with the droplet bulk, and the outer side

502   stretching forward. Since the precursor film typically extends more on hydrophilic substrates than

503   that on hydrophobic ones, the precursor film develops more rapidly, and the triple contact line thus

504   advances further, which is put forward as an additional mechanism for the greater droplet spreading

505   observed on hydrophilic substrates.

5. CONCLUSIONS

507   The present study provides novel fundamental insights in vapor absorption process into single

508   liquid hygroscopic desiccant droplets providing a new sub-topic of research on droplets. The effect

509   of substrate wettability and ambient conditions are explored. Typically, on hydrophilic glass

510   substrates, LiBr-H_2O droplets show a spreading trend during vapor absorption. While on

511   hydrophobic PTFE substrates, the smaller decrease in the contact angle along with an increasing

512   contact radius evidences the lower spreading behavior when compared to hydrophilic glass.

513   Moreover, the final volume expansion ratio of droplet is only function of relative humidity regardless

514   of ambient temperature and surface wettability.

515   Depending on the wettability of the substrate, the kinetics of vapor absorption are found to differ.

516   On hydrophilic glass substrates, LiBr-H_2O droplets reach equilibrium with the ambient much quicker

517   when compared to hydrophobic PTFE substrates. This is attributed to the shorter characteristic length

518 for solute diffusion, which is further demonstrated by evaluating the characteristic time for solute

519 diffusion within the droplet.

520   Besides, the apparent droplet spreading on hydrophilic glass substrates is explained based on a

521 force balance analysis at the triple contact line, by the evolution of liquid-gas droplet surface tension,

522 and by the development of a precursor film during vapor absorption.

523   To summarize, the vapor uptake into single liquid desiccant droplets and the mechanisms of

524 droplet growth and spreading are revealed. The presented findings are of great significance both for a

525 more accurate prediction of the vapor absorption process and for the optimization of

526 dehumidification devices.

527 **Conflict of Interests**

528 The authors declare that they have no conflict of interests.

529 **Acknowledgements**

535 **References**

536 [1] Park, J., & Moon, J. "Control of colloidal particle deposit patterns within picoliter droplets ejected
537   by ink-jet printing." *Langmuir* 22.8 (2006): 3506-3513.

Physical Chemistry Chemical Physics Accepted Manuscript

538   [2] Brinker, C. J., Lu, Y., Sellinger, A., & Fan, H. "Evaporation-induced self-assembly: nanostructures
539   made easy." *Advanced Materials* 11.7 (1999): 579-585.

540   [3] Ming, T., Kou, X., Chen, H., Wang, T., Tam, H. L., Cheah, K. W., Chen J. Y & Wang, J. "Ordered
541   gold nanostructure assemblies formed by droplet evaporation." *Angewandte Chemie* 120.50 (2008):
542   9831-9836.

543   [4] Dugas, V., Broutin, J., & Souteyrand, E. "Droplet evaporation study applied to DNA chip
544   manufacturing." *Langmuir* 21.20 (2005): 9130-9136.

545   [5] Sefiane, K., Wilson, S. K., David, S., Dunn, G. J., & Duffy, B. R. "On the effect of the atmosphere
546   on the evaporation of sessile droplets of water." *Physics of Fluids* 21.6 (2009): 062101.

547   [6] Sefiane, K. "Effect of nonionic surfactant on wetting behavior of an evaporating drop under a
548   reduced pressure environment." *Journal of Colloid and Interface Science* 272.2 (2004): 411-419.

549   [7] Girard, F., Antoni, M., Faure, S., & Steinchen, A. "Influence of heating temperature and relative
550   humidity in the evaporation of pinned droplets." *Colloids and Surfaces A: Physicochemical and
551   Engineering Aspects* 323.1 (2008): 36-49.

552   [8] Fukatani, Y., Orejon, D., Kita, Y., Takata, Y., Kim, J., & Sefiane, K. "Effect of ambient temperature
553   and relative humidity on interfacial temperature during early stages of drop evaporation." *Physical
554   Review E* 93.4 (2016): 043103.

555   [9] McHale, G., Aqil, S., Shirtcliffe, N. J., Newton, M. I., & Erbil, H. Y. "Analysis of droplet
556   evaporation on a superhydrophobic surface." *Langmuir* 21.24 (2005): 11053-11060.

557   [10] Patil, N. D., Bange, P. G., Bhardwaj, R., & Sharma, A. "Effects of substrate heating and wettability
558   on evaporation dynamics and deposition patterns for a sessile water droplet containing colloidal
559   particles." *Langmuir* 32.45 (2016): 11958-11972.

560   [11] Dunn, G. J., Wilson, S. K., Duffy, B. R., David, S., & Sefiane, K. "The strong influence of substrate
561   conductivity on droplet evaporation." *Journal of Fluid Mechanics* 623 (2009): 329-351.

562   [12] Zhong, X., & Duan, F. "Disk to dual ring deposition transformation in evaporating nanofluid
563   droplets from substrate cooling to heating." *Physical Chemistry Chemical Physics* 18.30 (2016):
564   20664-20671.

565   [13] Bansal, L., Chakraborty, S., & Basu, S. "Confinement-induced alterations in the evaporation
566   dynamics of sessile droplets." *Soft Matter* 13.5 (2017): 969-977.

567   [14] Xu, W., Leeladhar, R., Kang, Y. T., & Choi, C. H. "Evaporation kinetics of sessile water droplets on
568   micropillared superhydrophobic surfaces." *Langmuir* 29.20 (2013): 6032-6041.

569   [15] Askounis, A., Orejon, D., Koutsos, V., Sefiane, K., & Shanahan, M. E. "Nanoparticle deposits near
570   the contact line of pinned volatile droplets: size and shape revealed by atomic force
571   microscopy." *Soft Matter* 7.9 (2011): 4152-4155.

572   [16] Orejon, D., Sefiane, K., & Shanahan, M. E. "Stick–slip of evaporating droplets: substrate
573   hydrophobicity and nanoparticle concentration." *Langmuir* 27.21 (2011): 12834-12843.

Physical Chemistry Chemical Physics Accepted Manuscript

574 [17] Antonini, C., Lee, J. B., Maitra, T., Irvine, S., Derome, D., Tiwari, M. K., Carmeliet, J., Poulikakos,
575   D. "Unraveling wetting transition through surface textures with X-rays: Liquid meniscus penetration
576   phenomena." *Scientific Reports* 4 (2014): 4055.

577 [18] Popov, Y. O. "Evaporative deposition patterns: Spatial dimensions of the deposit." *Physical Review*
578   *E* 71 (2005): 036313.

579 [19] Shanahan, M. E. R., Sefiane, K., & Moffat, J. R., "Dependence of Volatile Droplet Lifetime on the
580   Hydrophobicity of the Substrate." *Langmuir* 27.8 (2011): 4572-4577.

581 [20] Stauber, J. M., Wilson, S. K., Duffy, B. R., & Sefiane, K. "On the lifetimes of evaporating droplets."
582   *Journal of Fluid Mechanics* 744 (2014): R2.

583 [21] Stauber, J. M., Wilson, S. K., Duffy, B. R., Sefiane, K., "On the lifetimes of evaporating droplets
584   with related initial and receding contact angles." *Physics of Fluids* 27 (2015): 122101.

585 [22] Schofield, F. G. H., Wilson, S. K., Pritchard, D., Sefiane, K., "The lifetimes of evaporating sessile
586   droplets are significantly extended by strong thermal effects." *Journal of Fluid Mechanics* 851
587   (2018): 231—244.

588 [23] Saada, M. A., Chikh, S., & Tadrist, L., "Evaporation of a sessile drop with pinned or receding
589   contact line on a substrate with different thermophysical properties" *International Journal of Heat*
590   *and Mass Transfer* 58 (2013):197-208.

591 [24] Mei, L., & Dai, Y. J. "A technical review on use of liquid-desiccant dehumidification for
592   air-conditioning application." *Renewable & Sustainable Energy Reviews* 12.3 (2008):662-689.

593 [25] Chua, K. J., Chou, S. K., & Yang, W. M. "Advances in heat pump systems: A review." *Applied*
594   *Energy* 87.12 (2010): 3611-3624.

595 [26] Wang, Z., Zhang, X., & Li, Z. "Evaluation of a flue gas driven open absorption system for heat and
596   water recovery from fossil fuel boilers." *Energy Conversion and Management* 128 (2016): 57-65.

597 [27] Parham, K., Khamooshi, M., Tematio, D. B. K., Yari, M., & Atikol, U. "Absorption heat
598   transformers–a comprehensive review." *Renewable and Sustainable Energy Reviews* 34 (2014):
599   430-452.

600 [28] Chua, K. J., Chou, S. K., & Yang, W. M. "Liquid desiccant materials and dehumidifiers – A
601   review." *Renewable & Sustainable Energy Reviews* 56 (2016):179-195.

602 [29] Hu, H., & Larson, "Evaporation of a sessile droplet on a substrate." *The Journal of Physical*
603   *Chemistry B* 106.6 (2002): 1334-1344.

604 [30] Liu, X. H., Zhang, Y., Qu, K. Y., & Jiang, Y. "Experimental study on mass transfer performances of
605   cross flow dehumidifier using liquid desiccant." *Energy Conversion and Management* 47.15 (2006):
606   2682-2692.

607 [31] Longo, G. A., & Gasparella, A. "Experimental and theoretical analysis of heat and mass transfer in a
608   packed column dehumidifier/regenerator with liquid desiccant." *International Journal of Heat and*
609   *Mass Transfer* 48.25 (2005): 5240-5254.

610   [32] Dai, Y. J., & Zhang, H. F. "Numerical simulation and theoretical analysis of heat and mass transfer
611   in a cross flow liquid desiccant air dehumidifier packed with honeycomb paper." *Energy Conversion*
612   *and Management* 45.9 (2004): 1343-1356.

613   [33] Al-Farayedhi, A. A., Gandhidasan, P., & Al-Mutairi, M. A. "Evaluation of heat and mass transfer
614   coefficients in a gauze-type structured packing air dehumidifier operating with liquid
615   desiccant." *International Journal of Refrigeration* 25.3 (2002): 330-339.

616   [34] Liu, X. H., Chang, X. M., Xia, J. J., & Jiang, Y. "Performance analysis on the internally cooled
617   dehumidifier using liquid desiccant." *Building and Environment* 44.2 (2009): 299-308.

618   [35] Yin, Y., Zhang, X., Wang, G., & Luo, L. "Experimental study on a new internally cooled/heated
619   dehumidifier/regenerator of liquid desiccant systems." *International Journal of Refrigeration* 31.5
620   (2008): 857-866.

621   [36] Wang, Z., Zhang, X., & Li, Z. "Investigation on the coupled heat and mass transfer process between
622   extremely high humidity air and liquid desiccant in the counter-flow adiabatic packed
623   tower." *International Journal of Heat and Mass Transfer* 110 (2017): 898-907.

624   [37] Jain, S., Tripathi, S., & Das, R. S. "Experimental performance of a liquid desiccant dehumidification
625   system under tropical climates." *Energy Conversion and Management* 52.6 (2011): 2461-2466.

626   [38] Luo, Y., Yang, H., Lu, L., & Qi, R. "A review of the mathematical models for predicting the heat
627   and mass transfer process in the liquid desiccant dehumidifier." *Renewable and Sustainable Energy*
628   *Reviews* 31 (2014): 587-599.

629   [39] Jeong, S., Garimella, S. "Falling-film and droplet mode heat and mass transfer in a horizontal tube
630   LiBr/water absorber." *International Journal of Heat and Mass Transfer*, 45.7 (2002): 1445-1458.

631   [40] Abdul-Wahab, S. A., Abu-Arabi, M. K., & Zurigat, Y. H. "Effect of structured packing density on
632   performance of air dehumidifier." *Energy Conversion and Management* 45.15-16 (2004):
633   2539-2552.

634   [41] Bonn, D., Eggers, J., Indekeu, J., Meunier, J., & Rolley, E. "Wetting and spreading." *Review of*
635   *Modern Physics* 81.2 (2009):739-805.

636   [42] Liu, C., Bonaccurso, E., & Butt, H. J. "Evaporation of sessile water/ethanol drops in a controlled
637   environment." *Physical Chemistry Chemical Physics* 10.47 (2008): 7150-7157.

638   [43] Qu, X., Davis, E.J., Swanson, B.D., "Non-isothermal droplet evaporation and condensation in the
639   near-continuum regime", *Journal of Aerosol Science* 32.11 (2001): 1315-1339.

640   [44] Kita, Y., Okauchi, Y., Fukatani, Y., Orejon, D., Kohno, M., Takata, Y., Sefiane, K. "Quantifying
641   vapor transfer into evaporating ethanol drops in humid atmosphere." *Physical Chemistry Chemical*
642   *Physics* 20 (2018): 19430-19440.

643   [45] Nath, S., Bisbano, C. E., Yue, P., Boreyko, J. "Duelling dry zones around hygroscopic droplets."
644   *Journal of Fluid Mechanics* 855 (2018): 601-620.

645   [46] Wimby, J. M., & Berntsson, T. S. "Viscosity and density of aqueous solutions of lithium bromide,
646   lithium chloride, zinc bromide, calcium chloride and lithium nitrate. 1. Single salt
647   solutions." *Journal of Chemical and Engineering Data* 39.1 (1994): 68-72.

Physical Chemistry Chemical Physics Accepted Manuscript

648 [47] Hopkins, R. J., & Reid, J. P. "Evaporation of ethanol/water droplets: examining the temporal
649   evolution of droplet size, composition and temperature." *The Journal of Physical Chemistry*
650   *A* 109.35 (2005): 7923-7931.

651 [48] Christy, J.R.E., Hamamoto, Y., Sefiane, K. "Flow Transition within an Evaporating Binary Mixture
652   Sessile Drop" *Physics Review Letters* 106 (2011): 205701.

653 [49] Dehaeck, S., Wylock, C., Colinet, P. "Evaporating cocktails" *Physics of Fluids* 21 (2009): 091108.

654 [50] Cussler, E. L. *Diffusion: Mass Transfer in Fluid Systems*. Cambridge University Press (Cambridge
655   Series in Chemical Engineering), 2009.

656 [51] Lobo, V. M. M., Ribeiro, A. C. F., & Verissimo, L. M. P. "Diffusion coefficients in aqueous
657   solutions of potassium chloride at high and low concentrations." *Journal of Molecular Liquids*
658   78.1-2 (1998): 139-149.

659 [52] Harned, H. S., & Levy, A. L. "The Differential Diffusion Coefficient of Calcium Chloride in Dilute
660   Aqueous Solutions at 25°." *Journal of the American Chemical Society* 71.8 (1949): 2781-2783.

661 [53] Mitra, S., & Mitra, S. K. "Understanding the early regime of drop spreading." *Langmuir* 32.35
662   (2016): 8843-8848.

663 [54] Tanner, L. H. "The spreading of silicone oil drops on horizontal surfaces." *Journal of Physics D:*
664   *Applied Physics* 12.9 (1979): 1473.

665 [55] Ruiter, R., Colinet, P., Brunet, P., Snoeijer, J.H., Gelderblom, H. "Contact line arrest in solidifying
666   spreading drops" *Physical Review Fluids* 2 (2017): 043602.

667 [56] Shanahan, M. E. R. "Meniscus Shape and contact angle of a slightly deformed axisymmetric drop."
668   *J. Phys. D: Appl. Phys.* 22 (1989): 1128-1135.

669 [57] Shanahan, M. E. R. "Simple Theory of "Stick-Slip" Wetting Hysteresis." *Langmuir* 11.3 (1995):
670   1041-1043.

671 [58] Shanahan, M. E. R. and Sefiane, K. "Contact Angle Wettability and Adhesion." *Taylor & Francis*
672   *Group Koninklijke Brill NV Leiden The Netherlands by K. L. Mittal* 6 (2009): 19-32.

673 [59] Young, T. "An essay on the cohesion of fluids." *Philosophical Transactions of the Royal Society of*
674   *London* 95 (1805): 65-87.

675 [60] Yao, W., Bjurstroem, H., & Setterwall, F. "Surface tension of lithium bromide solutions with
676   heat-transfer additives." *Journal of Chemical and Engineering Data* 36.1 (1991): 96-98.

677 [61] Gittens, G. J. "Variation of surface tension of water with temperature." *Journal of Colloid and*
678   *Interface Science* 30.3 (1969): 406-412.

679 [62] Tarasevich, Y.I. & Aksenenko, E.V. J. "Interaction of water molecules with hydrophilic and
680   hydrophobic surfaces of colloid particles." *Journal of Water Chemistry and Technology* 37.5 (2015):
681   224-229.

682 [63] Bernett, Marianne K., and W. A. Zisman. "Effect of adsorbed water on wetting properties of
683   borosilicate glass, quartz, and sapphire." *Journal of Colloid and Interface Science* 29.3 (1969):
684   413-423.

685   [64] Chengara, A., Nikolov, A. D., & Wasan, D. T. "Spreading of a water drop triggered by the surface
686   tension gradient created by the localized addition of a surfactant." *Industrial & Engineering*
687   *Chemistry Research* 46.10 (2007): 2987-2995.

688   [65] Bertozzi, A. L., Münch, A., Fanton, X., & Cazabat, A. M. "Contact line stability and
689   "undercompressive shocks" in driven thin film flow." *Physical Review Letters* 81.23 (1998): 5169.

690   [66] Leger, L., Erman, M., Guinet-Picard, A. M., Ausserre, D., & Strazielle, C. "Precursor film profiles
691   of spreading liquid drops." *Physical Review Letters* 60.23 (1988):2390-2393.

692   [67] Kavehpour, H. P., Ovryn, B., & McKinley, G. H. "Microscopic and Macroscopic Structure of the
693   Precursor Layer in Spreading Viscous Drops." *Physical Review Letters* 91.19 (2003):196104.

694   [68] Colinet, P., Rednikov, A. "Chapter 4 – Precursor Films and Contact Line Microstructures" *Droplet*
695   *Wetting and Evaporation*, Oxford (2015):31-56.

696   [69] Xu, H., Shirvanyants, D., Beers, K., Matyjaszewski, K., Rubinstein, M., & Sheiko, S. S. "Molecular
697   motion in a spreading precursor film." *Physical Review Letters* 93.20 (2004): 206103.

698   [70] Hoang, A., & Kavehpour, H. P. "Dynamics of nanoscale precursor film near a moving contact line
699   of spreading drops." *Physical Review Letters* 106.25 (2011):254501.

700   [71] Ghiradella, H., Radigan, W., & Frisch, H. L. "Electrical resistivity changes in spreading liquid
701   films." *Journal of Colloid and Interface Science* 51.3 (1975): 522-526.

702   [72] Carré, A., Gastel, J. C., & Shanahan, M. E. "Viscoelastic effects in the spreading of
703   liquids." *Nature* 379 (1996):432-434.

704

705   **TOC**
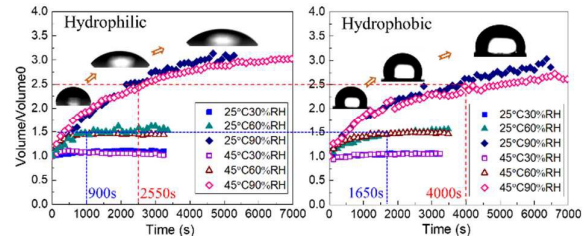
707   Mechanisms of droplet growth and spreading, related to surface wettability, are investigated during vapor
708   absorption into hygroscopic lithium-bromide desiccant droplets.